

Quark Degeneracy and the Lower Mass Gap

GREGORY L. FRAZIER¹

¹*Independent Researcher, Highland, Maryland, USA.*

ABSTRACT

The observed deficit of compact objects between ~ 2.5 and ~ 5 M_{\odot} —the lower mass gap—has no widely accepted physical explanation. We propose that the gap is the signature of the phase transition from neutron-degenerate to quark-degenerate matter, and present four lines of evidence: (1) the TOV equations predict the step-function jump in gravitational mass at the neutron→quark transition; (2) pulsars above the $2 M_{\odot}$ stability limit are observed only at fast spin rates, consistent with centrifugal support delaying collapse to black hole; (3) failed supernovae confirm that cores well below $5 M_{\odot}$ collapse; and (4) analysis of LIGO black hole merger data reveals spin-dependent mass deficits consistent with black holes being structured matter (versus being singularities). Stellar objects (neutron stars, red supergiant cores) of $\sim 2 M_{\odot}$ in size collapse to form black holes, and the smallest observed black hole is over $5 M_{\odot}$. There is no baryonic mass gap—the gap is in the observed, gravitational mass and is an inevitable result of the increased pressure that results from the collapse. And the existence of pressure means that black holes cannot be singularities.

Keywords: neutron stars, black holes, mass gap, quark stars, pulsars, gravitational waves, black hole mergers

Email: glfrazier@alum.mit.edu

20

1. INTRODUCTION

21 Gravitational-wave and X-ray observations reveal a gap in the mass spectrum of compact objects.
 22 Neutron stars with dynamically measured masses cluster below $\sim 2.5 M_{\odot}$ (J. M. Lattimer 2026),
 23 while black holes in X-ray binaries begin near $\sim 5 M_{\odot}$ (C. D. Bailyn et al. 1998). The deficit of
 24 objects between these limits is the *lower mass gap*.

25 The reality and origin of the gap have been debated for two decades. C. D. Bailyn et al. (1998)
 26 first identified the clustering of X-ray binary black holes above $\sim 5 M_{\odot}$; F. Özel et al. (2010) argued
 27 on statistical grounds that the gap is real and not a selection effect, and W. M. Farr et al. (2011)
 28 reached the same conclusion with a Bayesian analysis. L. Kreidberg et al. (2012) countered that
 29 systematic errors in X-ray binary mass measurements could partially fill the gap. On the theoretical
 30 side, C. L. Fryer et al. (2012) showed that rapid supernova explosion mechanisms can produce a gap
 31 by ejecting the envelope before significant fallback, while delayed mechanisms fill it in. More recently,
 32 the LIGO–Virgo detection of GW190814—a merger whose $2.6 M_{\odot}$ secondary sits squarely in the gap
 33 (R. Abbott et al. 2020)—and population synthesis studies (M. Zevin et al. 2020) have renewed the
 34 question of whether the gap is truly empty or merely underpopulated. No consensus has emerged on
 35 the physical origin of the deficit.

36 We propose that the lower mass gap is the signature of a phase transition. When a neutron star
 37 exceeds the Tolman-Oppenheimer-Volkoff (TOV) stability limit, its matter collapses from neutron
 38 degeneracy to quark degeneracy, producing a step-function increase in compactness, pressure, and
 39 thus gravitational mass. But the TOV equations not only predict the increase in gravitational mass—
 40 they also predict that, at the point where a neutron star collapses, the result is a black hole. The
 41 pressure contribution to gravitational mass cannot operate if the mass exists as a dimensionless point.
 42 As such, this explanation requires that black holes are not singularities but structured bodies—objects
 43 with a real equation of state, finite volume, and internal pressure inside the event horizon. This is a
 44 testable requirement; if black holes have internal structure, their mergers should exhibit signatures
 45 inconsistent with point-mass predictions. Thus we present four lines of evidence: TOV equations
 46 predict the gap (§2); massive pulsars (§3.1) and the pulsar population (§3.2) show the expected

⁴⁷ spin-dependent disappearance; failed supernovae independently confirm sub- $5 M_{\odot}$ collapse of objects
⁴⁸ to black holes (§3.3); and LIGO merger remnants carry spin signatures consistent with structured
⁴⁹ matter, in contrast to point singularities (§4).

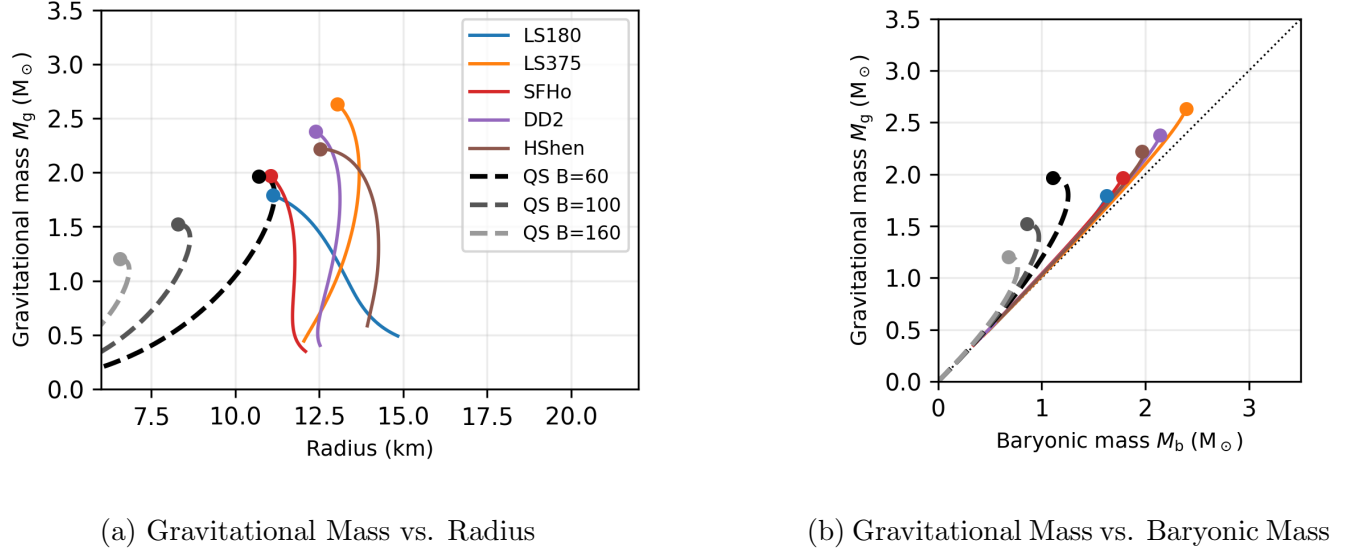
⁵⁰ 2. TOV EQUATION ANALYSIS

⁵¹ The Tolman–Oppenheimer–Volkoff equations (R. C. Tolman 1939; J. R. Oppenheimer & G. M.
⁵² Volkoff 1939) govern the hydrostatic structure of a self-gravitating, spherically symmetric body in
⁵³ general relativity. In particular, the pressure gradient equation,

$$\frac{dP}{dr} = -\frac{(\rho + P/c^2)(m + 4\pi r^3 P/c^2)G}{r(r - 2Gm/c^2)}, \quad (1)$$

⁵⁴ contains terms in which the pressure P itself contributes to the source of gravity. As a consequence,
⁵⁵ the gravitational mass of a compact star—the mass that determines its orbit and gravitational field—
⁵⁶ exceeds its baryonic (rest) mass: $M_g > M_b$. We define M_g as the total gravitational mass enclosed at
⁵⁷ the stellar surface. The baryonic mass M_b is defined so as to isolate the ground-state structural energy
⁵⁸ of each matter type, excluding the internal kinetic energy that generates pressure. For neutron-star
⁵⁹ matter, M_b is the integral of the baryon rest-mass density ρ_0 over coordinate volume—the mass the
⁶⁰ baryons would have if dispersed to infinity with zero internal energy. For quark-star matter, M_b is
⁶¹ the integral of the bag vacuum energy density $4B/c^2$ over coordinate volume—the QCD vacuum cost
⁶² of creating the quark-matter volume, with no quark kinetic contribution. Both definitions strip the
⁶³ internal energy that generates pressure and keep only the structural ground state. The difference
⁶⁴ $M_g - M_b$ then measures pressure’s contribution to the gravitating mass for both matter types, and
⁶⁵ grows with compactness.

⁶⁶ The relationship between pressure, density, and composition is encoded in the equation of state
⁶⁷ (EOS). For neutron-star matter, we adopt six finite-temperature nuclear EOS tables from the
⁶⁸ [stellarcollapse.org](#) repository (E. O’Connor & C. D. Ott 2010), evaluated on the cold, beta-
⁶⁹ equilibrated slice: LS180, LS220, and LS375 (J. M. Lattimer & F. D. Swesty 1991), SFHo (A. W.
⁷⁰ Steiner et al. 2013), DD2 (S. Typel et al. 2010), and HShen (H. Shen et al. 1998). These span the
⁷¹ range from soft (LS180, $K = 180$ MeV) to stiff (LS375, $K = 375$ MeV) nuclear incompressibil-
⁷²



(a) Gravitational Mass vs. Radius

(b) Gravitational Mass vs. Baryonic Mass

Figure 1. Neutron and Quark Star Stable Configurations

Solid curves are the six nuclear EOS; the dashed curves are MIT bag model quark stars with $B = 60, 100$, and 160 MeV/fm^3 . For a given baryonic mass M_b , quark stars have greater gravitational mass M_g than do neutron stars.

ties, producing maximum neutron-star masses of roughly $2.0\text{--}3.0 M_\odot$. For quark-star matter we use the MIT bag model (A. Chodos et al. 1974) with three representative bag constants, $B = 60, 100$, and 160 MeV/fm^3 , spanning the range from soft to stiff quark matter. These produce maximum gravitational masses of roughly $2.0, 1.6$, and $1.2 M_\odot$, respectively. While pure quark stars remain theoretical, recent Bayesian analyses of neutron-star observations find strong evidence for quark-matter cores above $\sim 2 M_\odot$ (E. Annala et al. 2020).

Figure 1a shows the standard mass-radius diagram obtained by integrating Eq. (1) across a range of central pressures for each EOS. The neutron-star branches span radii of $\sim 11\text{--}15 \text{ km}$, while the quark-star branches are more compact, reaching $\sim 7\text{--}11 \text{ km}$ at maximum mass depending on B . Both families terminate at a maximum gravitational mass beyond which no stable equilibrium exists.

The key result is shown in Figure 1b, which plots M_g against M_b . Every TOV solution sits above the $M_g = M_b$ line; the departure grows with compactness. The neutron-star curves (solid) hug the diagonal, with the pressure contribution amounting to $\sim 10\text{--}15\%$ of M_g at maximum mass. The quark-star curves (dashed) depart dramatically: because the baryonic mass counts only the bag

87 vacuum energy ($4B/c^2$), the entire ultrarelativistic quark kinetic energy ($3P/c^2$) appears as excess
 88 gravitational mass. At the quark-star maximum, $M_g/M_b \sim 1.5\text{--}2$, meaning that pressure-generated
 89 energy accounts for roughly half the gravitating mass.

90 The implications for the mass gap are direct. When a neutron star exceeds its TOV limit, it collapses
 91 from neutron-degenerate to quark-degenerate matter. The baryonic mass is conserved, but because
 92 the resulting quark star is more compact, its pressure contribution to M_g is larger: the gravitational
 93 mass jumps upward. The lower mass gap—the observed deficit of compact objects between ~ 2.5 and
 94 $\sim 5 M_\odot$ (F. Özel et al. 2010; W. M. Farr et al. 2011)—is the signature of this transition, spanning
 95 from the pre-collapse neutron-star M_g to the post-collapse quark-star M_g . Crucially, the post-collapse
 96 gravitational mass exceeds the maximum stable quark-star solution: the object is not a quark star but
 97 a black hole. Yet, the smallest observed black holes are over $5 M_\odot$, suggesting that black holes have
 98 a pressure component to their M_g , which in turn implies that they are coherent stellar objects—they
 99 are quark stars.

100 The spread of EOS and bag constants in Fig. 1 reflects current uncertainty in dense-matter physics;
 101 the precise behavior of matter at these densities is not yet known. Nonetheless, the qualitative
 102 picture is robust. Both families show a steepening M_g – M_b relationship with increasing baryonic
 103 mass, and quark stars consistently exhibit a far larger pressure contribution to M_g than neutron
 104 stars at comparable M_b .

105 This pressure contribution to M_g is not merely a theoretical refinement; it is an observable that
 106 distinguishes structured objects from singularities. A point singularity has zero volume, no equation
 107 of state, and no internal pressure—the TOV mechanism cannot operate. If black holes are singulari-
 108 ties, their gravitational mass equals their baryonic mass by construction. The fact that the smallest
 109 observed black holes sit well above the neutron star maximum implies a pressure contribution, and
 110 therefore internal structure.

111 That said, the TOV analysis demonstrates only that a phase transition *would* produce a mass gap
 112 whose endpoint is a black hole; it does not, by itself, show that neutron stars *do* collapse. Indeed, the

¹¹³ absence of a stable post-collapse solution might be read as evidence against collapse. Observational
¹¹⁴ evidence that collapse is occurring is presented in the following section.

¹¹⁵ 3. OBSERVATIONAL EVIDENCE FOR COLLAPSE

¹¹⁶ The TOV analysis predicts that neutron stars exceeding the stability limit collapse through the
¹¹⁷ mass gap into quark-degenerate configurations. This section presents three independent lines of
¹¹⁸ evidence that such collapses are occurring: the spin-dependent disappearance of massive pulsars, the
¹¹⁹ thinning of the pulsar population at long spin periods, and the failed-supernova phenomenon in red
¹²⁰ supergiants.

¹²¹ 3.1. *Pulsars with Known Mass*

¹²² We assemble a sample of 37 pulsars with dynamically measured masses from the
¹²³ stellarcollapse.org compilation ([E. O'Connor & C. D. Ott 2010](#)), cross-matched with spin peri-
¹²⁴ ods from the Australia Telescope National Facility (ATNF) Pulsar Catalogue ([R. N. Manchester et al.](#)
¹²⁵ [2005](#)). The sample spans $1.18\text{--}2.74 M_{\odot}$ and includes four binary categories: NS–WD (21 systems),
¹²⁶ NS–NS (7), X-Ray/Optical (2), and NS–MS (3). Three of the most precisely measured high-mass
¹²⁷ pulsars—J0740+6620 ($2.08 \pm 0.07 M_{\odot}$; [H. T. Cromartie et al. 2020](#)), J0348+0432 ($2.01 \pm 0.04 M_{\odot}$),
¹²⁸ and J1614–2230 ($1.928 \pm 0.017 M_{\odot}$)—anchor the high end of the distribution.

¹²⁹ Figure 2 reveals the key pattern. When the sample is binned by mass, the fastest spin period in
¹³⁰ each bin is comparable (1.61–2.56 ms), showing that millisecond pulsars exist at all masses. But
¹³¹ the slowest period shrinks dramatically: from 2773.5 ms in the $1.0\text{--}1.5 M_{\odot}$ bin down to 16.8 ms
¹³² above $2.5 M_{\odot}$. Massive pulsars are found exclusively at fast spin rates; no slowly rotating high-mass
¹³³ neutron star has been observed.

¹³⁴ This pattern is consistent with spin providing centrifugal support that delays collapse past the
¹³⁵ TOV stability limit. As pulsars spin down, those with the highest baryonic mass cross the stability
¹³⁶ boundary first, disappearing from the observable population. Only those massive pulsars that still
¹³⁷ retain fast spin remain visible. A Spearman rank correlation confirms the trend: $\rho = -0.41$ ($p =$
¹³⁸ 1.1×10^{-2}), indicating a statistically significant negative association between mass and spin period.

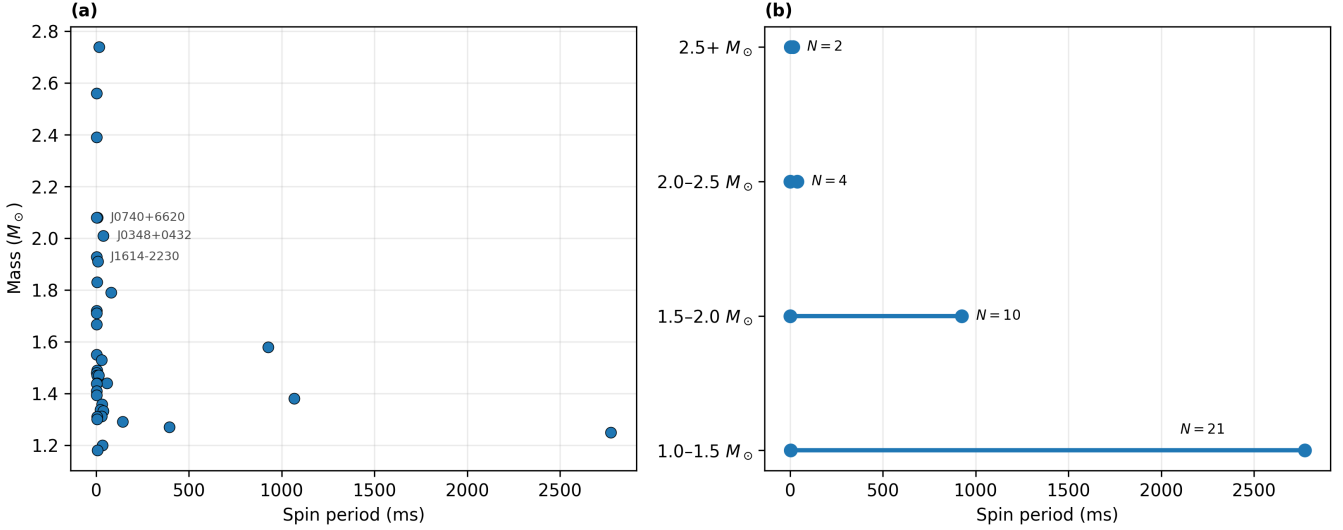


Figure 2. Mass vs. Spin Period, Pulsars with Known Mass

Examined 37 pulsars with dynamical mass measurements. (a) Scatter plot of 37 pulsars with known mass. No pulsar above $1.6 M_{\odot}$ has a slower period than 80 ms. (b) Period range per mass-bin: horizontal segments span from the fastest to the slowest period in each bin, with sample size annotated. The fastest periods are comparable across all bins (1.61–2.56 ms), but the slowest period drops from 2773 ms to 16.8 ms as mass increases. Note also that the number of pulsars in each bin decreases as the masses increase.

That said, these 37 pulsars are the subset with dynamically measured masses—a small, heterogeneous sample. The next subsection uses the full ATNF pulsar catalogue to test this interpretation with stronger statistics.

3.2. Pulsar Population Analysis

The preceding analysis showed that among pulsars with measured masses, the most massive are found exclusively at fast spin rates. If larger pulsars collapse as they spin down, the effect should leave a clear imprint on the period distribution of the full pulsar population.

We draw 4286 pulsars from the ATNF Pulsar Catalogue (R. N. Manchester et al. 2005) and restrict the sample to the 3305 normal (non-recycled) pulsars with $P \geq 100$ ms. Under magnetic dipole braking ($P\dot{P} \approx \text{const}$), the period derivative $\dot{P} \propto 1/P$, so pulsars traverse a given period interval more slowly at long periods. The dwell time in an interval dP scales as $P dP$, and in a steady-

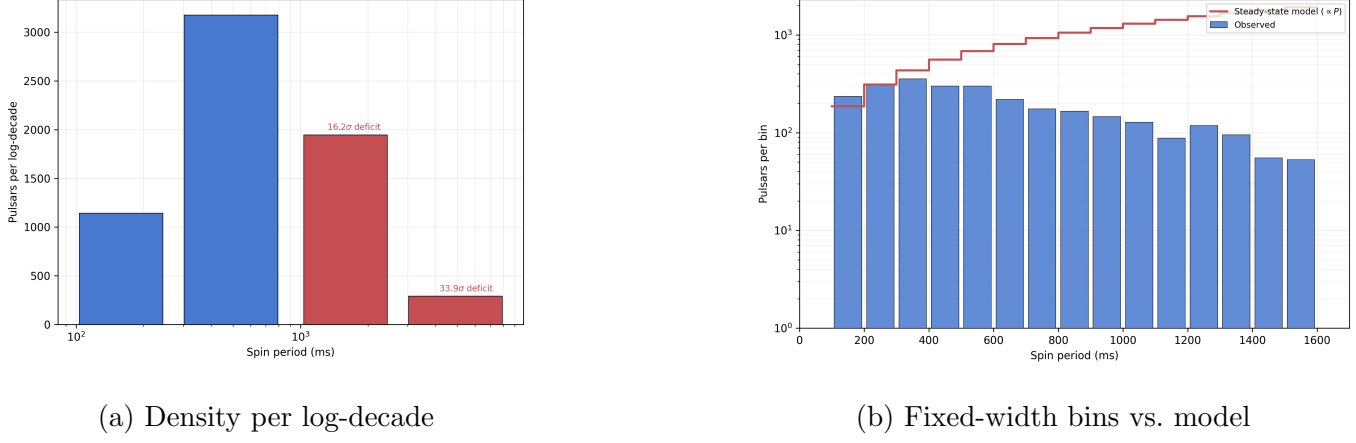


Figure 3. Period Distribution of Normal Pulsars ($P \geq 100$ ms)

(a) *Pulsars per log-decade in four logarithmically spaced bins. Blue bars are consistent with a non-decreasing density; red bars fall below the peak, with Poisson significance annotated.* (b) *Observed counts in 100 ms bins (blue) compared with the steady-state dipole spin-down prediction (count $\propto P$, red step line, normalised at 200–300 ms). Note the logarithmic vertical axis for (b).*

150 state population with constant birth rate the number density per log-decade of period should be
151 non-decreasing.

152 Figure 3a tests this prediction. The density rises from 1142 pulsars per decade in the 100–300 ms
153 bin to a peak of 3175 in the 300–1000 ms bin, then drops precipitously: 1947 in the 1000–3000 ms bin
154 (a 16.2σ deficit relative to the non-decreasing null) and just 293 in the 3000–10000 ms bin (33.9σ).
155 Figure 3b shows the same data in fixed-width bins alongside the steady-state prediction. The observed
156 counts fall exponentially while the model rises linearly; by 3 s the gap exceeds an order of magnitude.

157 The conventional explanation for the missing long-period pulsars is luminosity death: the cessation
158 of coherent radio emission below a critical spin-down power (C.-A. Faucher-Giguère & V. M. Kaspi
159 2006). However, the death line operates at $P \gtrsim 5$ s for typical magnetic fields and so does not account
160 for a population decline that is already observable at 0.1 s and is distributed across the entire range
161 of pulsar spin periods. Population synthesis studies have invoked magnetic field decay to fill the gap,
162 but the required timescales are uncertain and C.-A. Faucher-Giguère & V. M. Kaspi (2006) found
163 no evidence for significant field decay over pulsar lifetimes. Most recently, M. Sautron et al. (2024)
164 showed that a death line is not necessary to reproduce the observed $P-\dot{P}$ diagram: their simulations

with and without a death line are statistically indistinguishable once the maximum pulsar age is capped at $\sim 4 \times 10^7$ yr. What is required is simply that old pulsars are absent—but the physical reason for their absence remains unexplained in that framework.

The collapse hypothesis of §3.1 offers a natural explanation for observed population dynamics. As pulsars spin down, those with baryonic masses near the TOV limit lose centrifugal support and collapse to quark stars (black holes), physically removing them from the observable population. This predicts a gradual thinning of the population that begins well before the nominal death line—precisely the pattern seen in Figures 3a and 3b. It further predicts that the deficit should be strongest among the most massive pulsars, a test that targeted mass measurements at long periods could address.

3.3. The Red Supergiant Problem

The preceding subsections established that pulsars are disappearing from the observable population as they spin down—evidence that compact objects with baryonic mass well below $5 M_\odot$ are collapsing to form black holes. Here we examine a completely independent line of evidence that points to the same conclusion.

Red supergiants (RSGs) are massive evolved stars in the final stages of nuclear burning, with initial (zero-age main-sequence) masses of roughly $8\text{--}25 M_\odot$. Stars in this range are expected to end their lives as core-collapse supernovae. However, S. J. Smartt et al. (2009) analysed pre-explosion images of a volume-limited sample of Type II-P supernovae and found that no progenitor more massive than $16.5 \pm 1.5 M_\odot$ had been identified—despite RSGs with masses up to $\sim 25 M_\odot$ being well documented in the Local Group. An expanded sample of 45 progenitors confirmed the deficit: 13 high-luminosity progenitors were expected under a Salpeter initial mass function, but only one was found (S. J. Smartt 2015). This discrepancy—the absence of supernova progenitors in the $\sim 17\text{--}25 M_\odot$ range—is known as the *red supergiant problem*.

The natural explanation is that the most massive RSGs do not produce visible supernovae: their cores collapse directly to black holes, with the stellar envelope falling back rather than being ejected. C. S. Kochanek (2020) showed that this “failed supernova” hypothesis provides a consistent explanation for both the missing progenitors and the observed black hole mass function. A systematic

192 search by the Large Binocular Telescope survey, monitoring luminous stars in 27 nearby galaxies over
 193 11 years, estimates that $16^{+23\%}_{-12\%}$ of core-collapse events produce failed supernovae (J. M. M. Neustadt
 194 & C. S. Kochanek 2021).

195 Two candidate failed supernovae have now been identified observationally. NGC 6946-BH1, a
 196 $\sim 25 M_{\odot}$ red supergiant, underwent a brief optical outburst in 2009 and then vanished; by 2015
 197 it was undetectable in optical light (S. M. Adams et al. 2017), though subsequent JWST imaging
 198 revealed that the pre-disappearance source was a blend of at least three objects, complicating the
 199 interpretation (E. R. Beasor et al. 2024). The clearer case is M31-2014-DS1, a hydrogen-depleted
 200 supergiant in the Andromeda Galaxy (K. De et al. 2026). With an initial mass of $\sim 13 M_{\odot}$ —notably
 201 below the RSG problem threshold, extending the failed-supernova phenomenon to lower masses—and
 202 a terminal mass of $\sim 5 M_{\odot}$, this star faded by a factor of $\gtrsim 10^4$ in optical light between 2017 and
 203 2022 with no associated supernova. Modelling indicates that $\sim 98\%$ of the stellar mass collapsed or
 204 fell back, forming a $\sim 5 M_{\odot}$ black hole.

205 The implications for the mass gap are direct. Stellar evolution models show that the iron core
 206 mass at the point of collapse is $\sim 1.3\text{--}1.8 M_{\odot}$ across the entire range from 8 to $25 M_{\odot}$ (S. E. Woosley
 207 et al. 2002; T. Sukhbold et al. 2016). This is the mass that actually undergoes gravitational collapse;
 208 subsequent accretion of envelope material occurs only after the compact remnant has formed. Thus,
 209 the baryonic mass of the collapsing core is certainly less than $5 M_{\odot}$ and most likely less than $2 M_{\odot}$.

210 The failed-supernova evidence therefore establishes, independently of the pulsar analysis, that cores
 211 with baryonic mass well below $5 M_{\odot}$ —most likely $\sim 1.5 M_{\odot}$ —can and do collapse to form black holes.
 212 This is precisely the process proposed in §3.1 and §3.2 for pulsars that lose centrifugal support as they
 213 spin down. That the same phenomenon—black hole formation from a $\sim 2 M_{\odot}$ compact core—appears
 214 in two completely unrelated astrophysical settings strengthens the case that the lower mass gap is
 215 the signature of this collapse, as predicted by the TOV analysis of §2.

216 4. BLACK HOLE MERGER SPIN ANALYSIS

217 The preceding sections established that compact objects with baryonic mass well below $5 M_{\odot}$
 218 collapse to form black holes, and that the TOV equations predict a mass gap at the neutron–

quark transition. But those arguments do not, by themselves, demonstrate that black holes contain structured matter. If black holes are quark stars—compact objects with a real equation of state, finite radius, and internal pressure—then their mergers should leave observable signatures in the gravitational-wave record that differ from the predictions of the point-singularity model. The GWTC catalog (The LIGO Scientific Collaboration et al. 2023; R. Abbott et al. 2023) provides exactly the data needed to test this.

Consider two models of what happens when two black holes merge. In the singularity model, each black hole is a point mass enclosed by an event horizon; the mass deficit $m_1 + m_2 - m_{\text{final}}$ is energy radiated as gravitational waves. The “spin” of a Kerr black hole is a property of the spacetime geometry: angular momentum is defined as a conserved charge at spatial infinity, and the singularity itself has no moment of inertia and no internal structure for centrifugal force to act upon. In the quark star model, two physical objects collide and merge. The remnant is a spinning body with a moment of inertia, and its spin provides centrifugal support that reduces the internal pressure and therefore reduces the gravitational mass M_g relative to the conserved baryonic mass M_b . No baryonic mass is converted to energy—the gravitational-wave energy comes from the rotational kinetic energy of the inspiral—and the apparent mass deficit includes a spin-induced reduction in M_g .

The two models also differ in how they account for the gravitational waves observed after the merger (the “ringdown”). In the singularity model, the inspiral GWs are driven radiation, sourced by the stress-energy of orbiting masses; but the post-merger GWs are quasi-normal modes—source-free oscillations of the Kerr geometry ringing down to equilibrium. The radiation mechanism changes at merger from matter-sourced to geometry-sourced. In the quark star model, a single mechanism operates throughout: the time-varying quadrupole moment of a physical mass distribution, first from two bodies in mutual orbit, then from a distorted remnant settling into axial symmetry. Both models predict post-merger gravitational waves—quasi-normal modes have been a prediction of the Kerr model since the 1970s—but they disagree on what is radiating.

Both models predict that the mass deficit depends on the symmetric mass ratio $\eta = m_1 m_2 / (m_1 + m_2)^2$, because the orbital dynamics that govern both GW radiation and angular momentum transfer

are controlled by η . We use the spinning-GR prediction as a baseline, extending A. Buonanno et al. (2008) by replacing the Schwarzschild innermost stable circular orbit (ISCO) binding energy with its Kerr analogue (J. M. Bardeen et al. 1972):

$$f_{\text{GR}}(\eta, \chi_{\text{eff}}) = e_{\text{ISCO}}(\chi_{\text{eff}}) \eta + 0.498 \eta^2, \quad (2)$$

where $e_{\text{ISCO}}(\chi_{\text{eff}})$ is the analytic Kerr ISCO binding energy fraction; at $\chi_{\text{eff}} = 0$ it equals $1 - \sqrt{8/9} \approx 0.0572$, recovering the BKL non-spinning formula. The quark star model predicts additional deficit from spin-induced M_g reduction, proportional to the remnant spin generated.

We test this using 157 confident binary black hole events ($m_1 > 3 \text{ M}_\odot$, $m_2 > 3 \text{ M}_\odot$, $p_{\text{astro}} > 0.5$) from the GWTC catalog, of which 154 have both a measured final mass and effective spin χ_{eff} . For each event we compute the remnant spin χ_f from the numerical-relativity fitting formula

$$\chi_f = L_{\text{orb}}(\eta) + \frac{\chi_{\text{eff}} (1 + q^2)}{(1 + q)^2}, \quad (3)$$

where $L_{\text{orb}}(\eta) = 2\sqrt{3}\eta - 3.52\eta^2 + 2.58\eta^3$ is the orbital angular momentum contribution and the second term is the spin angular momentum contribution (assuming equal component spins $a_1 = a_2 = \chi_{\text{eff}}$). The excess fractional deficit is then $\Delta f = f_{\text{obs}} - f_{\text{GR}}$, where $f_{\text{obs}} = (m_1 + m_2 - m_{\text{final}})/(m_1 + m_2)$.

Test 1: excess deficit vs. remnant spin.

Figure 4 plots the excess fractional deficit Δf against the computed remnant spin χ_f for all 154 events. A Spearman rank correlation gives $\rho = +0.506$ ($p = 2.2 \times 10^{-11}$), a highly significant positive association. The median excess is 0.0029, and 84% of events exceed the spinning GR prediction. The binned medians trace a clear rising curve from near zero at $\chi_f \approx 0.55$ to ~ 0.012 at $\chi_f \approx 0.85$.

The quark star model offers a direct physical mechanism for this correlation: a spinning body with internal structure experiences centrifugal support that reduces its central pressure and therefore its gravitational mass. More remnant spin means more centrifugal support and a larger apparent mass deficit. In the singularity model, the remnant's "spin" is a geometric property of the Kerr metric, with no internal structure for centrifugal force to act upon; the connection between spin and mass deficit is less direct.

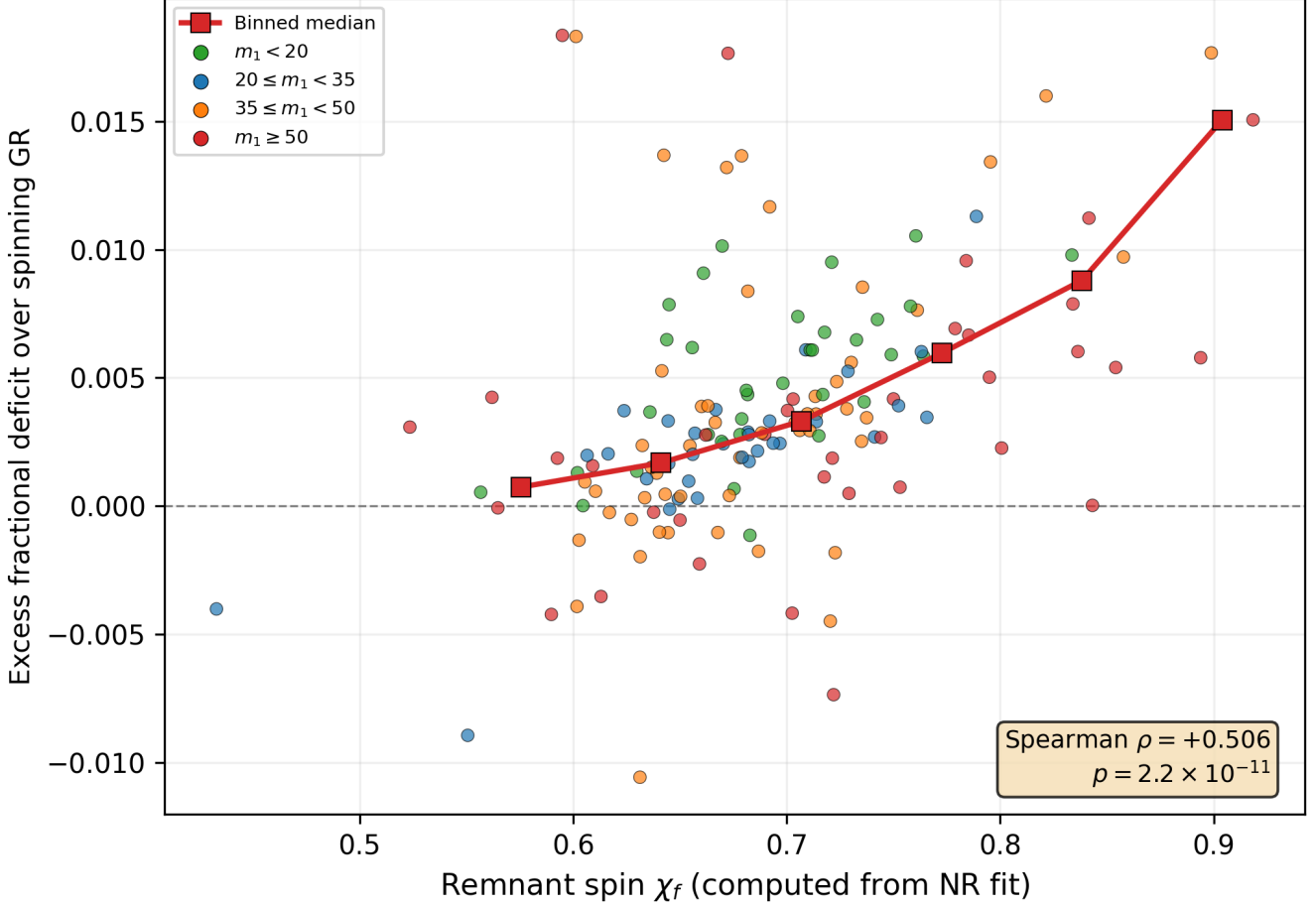


Figure 4. Excess Fractional Mass Deficit vs. Remnant Spin

Each point is a GWTC binary black hole merger. The excess is computed relative to the spinning GR prediction (Eq. 2). Points are coloured by primary mass m_1 . Remnant spin χ_f is computed from Eq. (3). Red squares show binned medians. The Spearman correlation ($\rho = +0.506$, $p = 2.2 \times 10^{-11}$) confirms that higher remnant spin is associated with larger excess deficit.

A natural concern is that the Test 1 correlation might partly reflect shared η -dependence: χ_f contains $L_{\text{orb}}(\eta)$ and f_{GR} also depends on η . In the GWTC sample, however, χ_f is dominated by the progenitor spin component $\chi_{\text{eff}}(1+q^2)/(1+q)^2$ (Spearman $\rho = +0.875$ with χ_f) rather than by $L_{\text{orb}}(\eta)$ ($\rho = +0.041$). More tellingly, η is *negatively* correlated with the excess ($\rho = -0.349$, $p = 9.0 \times 10^{-6}$), so the L_{orb} term dilutes rather than drives the Test 1 result. Using the progenitor spin component alone yields a stronger correlation ($\rho = +0.643$, $p = 2.6 \times 10^{-19}$); the partial Spearman correlation controlling for η gives $\rho = +0.556$ ($p = 7.4 \times 10^{-14}$); and the correlation is highly significant within

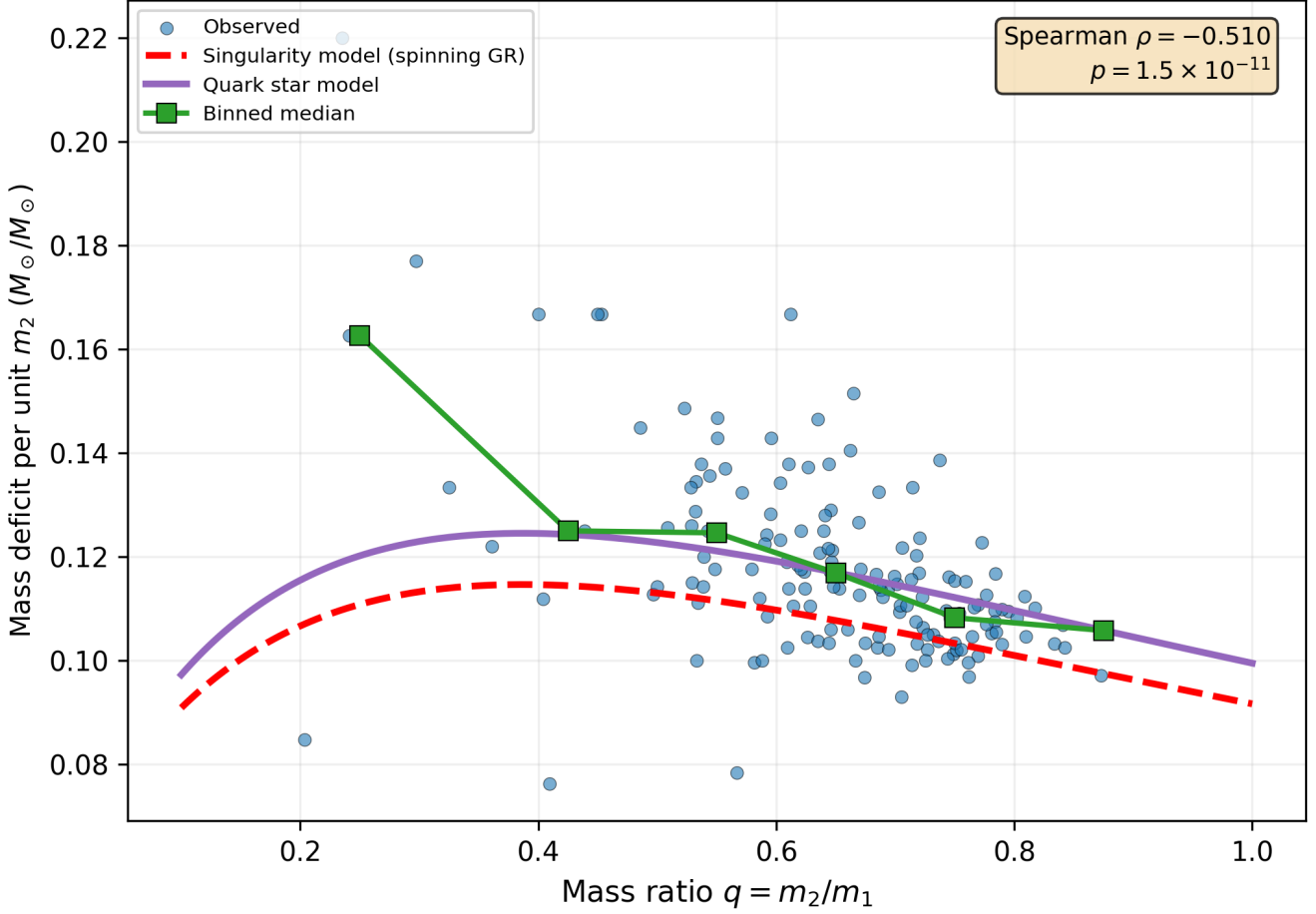


Figure 5. Mass Deficit per Unit m_2 vs. Mass Ratio

Blue points: observed deficit divided by m_2 for each GWTC event. Red dashed curve: singularity model (spinning GR, Eq. 2, at median χ_{eff}). Purple solid curve: quark star model, adding spin-induced M_g reduction with $\alpha = 0.0083$ fit from Test 1. Green squares: binned medians. The data follow the quark star prediction, not the singularity prediction ($\rho = -0.510$, $p = 1.5 \times 10^{-11}$).

278 each of three equal-sized η -tercile subsamples ($\rho \approx 0.45$ – 0.55 in each). There is no η -confound: the
279 excess tracks progenitor spin, not mass-ratio geometry.

280 *Test 2: deficit per unit m_2 vs. mass ratio.*

281 Figure 5 plots the total mass deficit per unit m_2 against the mass ratio q . The singularity model
282 curve (red, dashed) is the spinning GR baseline (Eq. 2) evaluated at the sample median $\chi_{\text{eff}} = 0.05$,
283 normalised by m_2 . The quark star model curve (purple, solid) adds the spin-induced M_g reduction,

²⁸⁴ $f_{\text{QS}} = f_{\text{GR}} + \alpha L_{\text{orb}}(\eta)^2$, using $\alpha = 0.0083$ taken directly from the Test 1 fit—a parameter-free
²⁸⁵ prediction for Test 2. Both curves share the same shape because GW radiation and spin deposition
²⁸⁶ are both governed by η ; the quark star curve is shifted uniformly upward because the decreasing L_{orb}^2
²⁸⁷ at low q is offset by the increasing $1/m_2$ amplification.

²⁸⁸ The binned medians (green squares) track the quark star curve across the full range of mass ratios,
²⁸⁹ sitting consistently above the singularity prediction ($\rho = -0.510$, $p = 1.5 \times 10^{-11}$). The quark star
²⁹⁰ model thus accounts for both tests with one physical mechanism—centrifugal support reducing M_g —
²⁹¹ and one free parameter (α) calibrated on Test 1 and applied unchanged to Test 2.

292 5. CONCLUSION

²⁹³ The lower mass gap between neutron stars and black holes has lacked a physical explanation. We
²⁹⁴ have argued that there is no baryonic mass gap. The gap is in gravitational mass and is the signature
²⁹⁵ of the phase transition from neutron degeneracy to quark degeneracy, driven by the same pressure–
²⁹⁶ gravity coupling embedded in the TOV equations. A direct implication is that black holes are not
²⁹⁷ singularities but structured stellar objects with finite volume, an equation of state, and internal
²⁹⁸ pressure that contributes to their gravitational mass.

²⁹⁹ Four independent lines of evidence support this picture. The TOV equations show that a neutron–
³⁰⁰ to-quark transition produces a gravitational-mass jump that anticipates the observed gap (§2). Mas-
³⁰¹ sive pulsars are found exclusively at fast spin rates, consistent with centrifugal support delaying
³⁰² collapse past the stability limit (§3.1). An assessment of the full observed pulsar population, for
³⁰³ which mass information is unavailable, shows that pulsars are disappearing from the population,
³⁰⁴ consistent with centrifugal support delaying collapse (§3.2). Failed supernovae confirm, indepen-
³⁰⁵ dently of the pulsar evidence, that stellar cores with baryonic mass well below $5 M_\odot$ collapse to form
³⁰⁶ black holes (§3.3). Finally, LIGO merger remnants show a spin-dependent mass deficit that correlates
³⁰⁷ with remnant spin and exceeds the spinning GR prediction by the amount a structured-matter model
³⁰⁸ predicts—with a single free parameter calibrated on one observable and applied to a second (§4).

³⁰⁹ Several directions for future work are apparent. Targeted mass measurements of long-period pulsars
³¹⁰ could test the prediction that the spin-down disappearance is strongest among the most massive

³¹¹ neutron stars. And the continued growth of the gravitational-wave catalog will improve the statistical
³¹² power of the merger analysis presented here.

³¹³ **ACKNOWLEDGMENTS**

³¹⁴ The author acknowledges the use of Claude (Anthropic) as an AI assistant in the development,
³¹⁵ analysis, and manuscript preparation of this work.

³¹⁶ **DATA AVAILABILITY**

³¹⁷ The data underlying this article are drawn from publicly available catalogs: the ATNF Pul-
³¹⁸ sar Catalogue (R. N. Manchester et al. 2005), the GWTC-3 gravitational-wave catalog (The
³¹⁹ LIGO Scientific Collaboration et al. 2023; R. Abbott et al. 2023), and equation-of-state tables
³²⁰ from stellarcollapse.org (E. O'Connor & C. D. Ott 2010). Analysis code is available at
³²¹ <https://github.com/glfrazier-42/MassGap>.

REFERENCES

- ³²² Abbott, R., Abbott, T. D., Abraham, S., et al. ³³⁵ Bailyn, C. D., Jain, R. K., Coppi, P., & Orosz,
³²³ 2020, The Astrophysical Journal Letters, 896, ³³⁶ J. A. 1998, The Astrophysical Journal, 499, 367,
³²⁴ L44, doi: [10.3847/2041-8213/ab960f](https://doi.org/10.3847/2041-8213/ab960f) ³³⁷ doi: [10.1086/305614](https://doi.org/10.1086/305614)
- ³²⁵ Abbott, R., et al. 2023, The Astrophysical Journal ³³⁸ Bardeen, J. M., Press, W. H., & Teukolsky, S. A.
³²⁶ Supplement Series, 267, 29, ³³⁹ 1972, The Astrophysical Journal, 178, 347,
³²⁷ doi: [10.3847/1538-4365/acdc9f](https://doi.org/10.3847/1538-4365/acdc9f) ³⁴⁰ doi: [10.1086/151796](https://doi.org/10.1086/151796)
- ³²⁸ Adams, S. M., Kochanek, C. S., Gerke, J. R., ³⁴¹ Beasor, E. R., Hosseinzadeh, G., Smith, N., et al.
³²⁹ Stanek, K. Z., & Dai, X. 2017, Monthly Notices ³⁴² 2024, The Astrophysical Journal, 964, 171,
³³⁰ of the Royal Astronomical Society, 468, 4968, ³⁴³ doi: [10.1093/mnras/stx816](https://doi.org/10.1093/mnras/stx816) doi: [10.3847/1538-4357/ad2df0](https://doi.org/10.3847/1538-4357/ad2df0)
- ³³² Annala, E., Gorda, T., Kurkela, A., Näyttlä, J., & ³⁴⁴ Buonanno, A., Kidder, L. E., & Lehner, L. 2008,
³³³ Vuorinen, A. 2020, Nature Physics, 16, 907, ³⁴⁵ Physical Review D, 77, 026004,
³³⁴ doi: [10.1038/s41567-020-0914-9](https://doi.org/10.1038/s41567-020-0914-9) ³⁴⁶ doi: [10.1103/PhysRevD.77.026004](https://doi.org/10.1103/PhysRevD.77.026004)

- 347 Chodos, A., Jaffe, R. L., Johnson, K., Thorn,
 348 C. B., & Weisskopf, V. F. 1974, Physical Review
 349 D, 9, 3471, doi: [10.1103/PhysRevD.9.3471](https://doi.org/10.1103/PhysRevD.9.3471)
- 350 Cromartie, H. T., Fonseca, E., Ransom, S. M.,
 351 et al. 2020, Nature Astronomy, 4, 72,
 352 doi: [10.1038/s41550-019-0880-2](https://doi.org/10.1038/s41550-019-0880-2)
- 353 De, K., MacLeod, M., Jencson, J. E., Lovegrove,
 354 E., et al. 2026, Science, 391, 689,
 355 doi: [10.1126/science.adt4853](https://doi.org/10.1126/science.adt4853)
- 356 Farr, W. M., Sravan, N., Cantrell, A., et al. 2011,
 357 The Astrophysical Journal, 741, 103,
 358 doi: [10.1088/0004-637X/741/2/103](https://doi.org/10.1088/0004-637X/741/2/103)
- 359 Faucher-Giguère, C.-A., & Kaspi, V. M. 2006, The
 360 Astrophysical Journal, 643, 332,
 361 doi: [10.1086/501516](https://doi.org/10.1086/501516)
- 362 Fryer, C. L., Belczynski, K., Wiktorowicz, G.,
 363 et al. 2012, The Astrophysical Journal, 749, 91,
 364 doi: [10.1088/0004-637X/749/1/91](https://doi.org/10.1088/0004-637X/749/1/91)
- 365 Kochanek, C. S. 2020, Monthly Notices of the
 366 Royal Astronomical Society, 493, 4945,
 367 doi: [10.1093/mnras/staa605](https://doi.org/10.1093/mnras/staa605)
- 368 Kreidberg, L., Bailyn, C. D., Farr, W. M., &
 369 Kalogera, V. 2012, The Astrophysical Journal,
 370 757, 36, doi: [10.1088/0004-637X/757/1/36](https://doi.org/10.1088/0004-637X/757/1/36)
- 371 Lattimer, J. M. 2026, Neutron Star Masses (online
 372 compilation),,
 373 <https://stellarcollapse.org/nsmasses>
- 374 Lattimer, J. M., & Swesty, F. D. 1991, Nuclear
 375 Physics A, 535, 331,
 376 doi: [10.1016/0375-9474\(91\)90452-C](https://doi.org/10.1016/0375-9474(91)90452-C)
- 377 Manchester, R. N., Hobbs, G. B., Teoh, A., &
 378 Hobbs, M. 2005, The Astronomical Journal,
 379 129, 1993, doi: [10.1086/428488](https://doi.org/10.1086/428488)
- 380 Neustadt, J. M. M., & Kochanek, C. S. 2021,
 381 Monthly Notices of the Royal Astronomical
 382 Society, 508, 516, doi: [10.1093/mnras/stab2605](https://doi.org/10.1093/mnras/stab2605)
- 383 O'Connor, E., & Ott, C. D. 2010, Classical and
 384 Quantum Gravity, 27, 114103,
 385 doi: [10.1088/0264-9381/27/11/114103](https://doi.org/10.1088/0264-9381/27/11/114103)
- 386 Oppenheimer, J. R., & Volkoff, G. M. 1939,
 387 Physical Review, 55, 374,
 388 doi: [10.1103/PhysRev.55.374](https://doi.org/10.1103/PhysRev.55.374)
- 389 Özel, F., Psaltis, D., Narayan, R., & McClintock,
 390 J. E. 2010, The Astrophysical Journal, 725,
 391 1918, doi: [10.1088/0004-637X/725/2/1918](https://doi.org/10.1088/0004-637X/725/2/1918)
- 392 Sautron, M., Pétri, J., Mitra, D., & Dirson, L.
 393 2024, Astronomy & Astrophysics, 691, A349,
 394 doi: [10.1051/0004-6361/202451097](https://doi.org/10.1051/0004-6361/202451097)
- 395 Shen, H., Toki, H., Oyamatsu, K., & Sumiyoshi,
 396 K. 1998, Nuclear Physics A, 637, 435,
 397 doi: [10.1016/S0375-9474\(98\)00236-X](https://doi.org/10.1016/S0375-9474(98)00236-X)
- 398 Smartt, S. J. 2015, Publications of the
 399 Astronomical Society of Australia, 32, e016,
 400 doi: [10.1017/pasa.2015.17](https://doi.org/10.1017/pasa.2015.17)
- 401 Smartt, S. J., Eldridge, J. J., Crockett, R. M., &
 402 Maund, J. R. 2009, Monthly Notices of the
 403 Royal Astronomical Society, 395, 1409,
 404 doi: [10.1111/j.1365-2966.2009.14506.x](https://doi.org/10.1111/j.1365-2966.2009.14506.x)
- 405 Steiner, A. W., Fischer, T., & Hempel, M. 2013,
 406 The Astrophysical Journal, 774, 17,
 407 doi: [10.1088/0004-637X/774/1/17](https://doi.org/10.1088/0004-637X/774/1/17)

- 408 Sukbold, T., Ertl, T., Woosley, S. E., Brown,
409 J. M., & Janka, H.-T. 2016, The Astrophysical
410 Journal, 821, 38,
411 doi: [10.3847/0004-637X/821/1/38](https://doi.org/10.3847/0004-637X/821/1/38)
- 412 The LIGO Scientific Collaboration, The Virgo
413 Collaboration, & The KAGRA Collaboration.
414 2023, Physical Review X, 13, 041039,
415 doi: [10.1103/PhysRevX.13.041039](https://doi.org/10.1103/PhysRevX.13.041039)
- 416 Tolman, R. C. 1939, Physical Review, 55, 364,
417 doi: [10.1103/PhysRev.55.364](https://doi.org/10.1103/PhysRev.55.364)
- 418 Typel, S., Röpke, G., Klähn, T., Blaschke, D., &
419 Wolter, H. H. 2010, Physical Review C, 81,
420 015803, doi: [10.1103/PhysRevC.81.015803](https://doi.org/10.1103/PhysRevC.81.015803)
- 421 Woosley, S. E., Heger, A., & Weaver, T. A. 2002,
422 Reviews of Modern Physics, 74, 1015,
423 doi: [10.1103/RevModPhys.74.1015](https://doi.org/10.1103/RevModPhys.74.1015)
- 424 Zevin, M., Spera, M., Berry, C. P. L., & Kalogera,
425 V. 2020, The Astrophysical Journal Letters,
426 899, L1, doi: [10.3847/2041-8213/aba74e](https://doi.org/10.3847/2041-8213/aba74e)